

# Tuning Band Tails in Mono- and Multilayered Transition-Metal Dichalcogenides: A Detailed Assessment and a Quick-Reference Guide

Prasad Sarangapani<sup>1,\*</sup>, James Charles,<sup>1</sup> and Tillmann Kubis<sup>1,2,3,4,5</sup>

<sup>1</sup>*School of Electrical and Computer Engineering, Purdue University, West Lafayette, Indiana 47907, USA*

<sup>2</sup>*Network for Computational Nanotechnology, Purdue University, West Lafayette, Indiana 47907, USA*

<sup>3</sup>*Purdue Center for Predictive Materials and Devices, Purdue University, West Lafayette, Indiana 47907, USA*

<sup>4</sup>*Purdue Institute of Inflammation, Immunology and Infectious Disease, Purdue University, West Lafayette, Indiana 47907, USA*

<sup>5</sup>*Purdue Quantum Science and Engineering Institute, West Lafayette, Indiana 47907, USA*



(Received 12 October 2021; revised 29 December 2021; accepted 10 January 2022; published 2 February 2022)

Transition-metal dichalcogenides (TMDs) are promising candidates for a wide variety of ultrascaled electronic, optoelectronic, and quantum-computing applications. The electronic density of states exponentially decaying into the band gap (also known as the band tail) has a strong impact on the performance of TMD applications. In this work, the band tails of various TMD monolayer and multilayer systems are predicted with density-functional-theory-based nonequilibrium Green's functions when placed on several dielectric substrates such as HfO<sub>2</sub>, Al<sub>2</sub>O<sub>3</sub>, SiO<sub>2</sub>, and *h*-BN. Nonlocal scattering of electrons on polar optical phonons, charged impurities, and remote scattering on phonons in the dielectric materials is included in the self-consistent Born approximation. The band tails are found to critically depend on the layer thickness, temperature, doping concentration, and particularly on the chosen dielectric substrate. The underlying physical mechanisms are studied in high detail and an analytical interpolation formula is given to provide a quick reference for Urbach parameters and to guide the design work in MoS<sub>2</sub>, WS<sub>2</sub>, and WSe<sub>2</sub>.

DOI: 10.1103/PhysRevApplied.17.024005

## I. INTRODUCTION

Two-dimensional materials have attracted considerable attention due to their unique electronic, optical, and mechanical properties [1–5]. Transition-metal dichalcogenides (TMDs) have a finite band gap making it an attractive alternative in electronics for Si/SiGe-based transistors [6–9], in optoelectronics as possible materials in light-emitting diodes [10–15] and solar-cell applications [16–18]. TMD layers are coupled by weak van der Waals forces, which allows for mechanical cleavage of bulk TMD materials into mono- and multilayer systems. These systems yield electronic and optical properties that depend strongly on the number of layers [19]. Stacking multiple TMD layers on top of each other significantly widens the available material design space [20,21] resulting in a plethora of ultrathin devices such as stacked optoelectronic *p-n* junctions [4,22,23], photovoltaics [24–26], as well as ultrascaled nonvolatile and neuromorphic memory devices [27–29]. Electrons in TMDs scatter on phonons, defects, and charged impurities, which leads to band tails (also known as Urbach tails), i.e., exponentially decaying density of states in the band gap [30–36]. The

slope of the exponential density of states' tail is known as the Urbach parameter. Urbach tails can significantly alter the device performance: the switching of transistors is drastically affected by these tails [37–39]. They affect the optical behavior such as absorption spectra and absorption-recombination coefficients in optoelectronic devices [40–42]. They also set a fundamental limit on the subthreshold performance of semiconductor devices at cryogenic temperatures for large-scale quantum-computing applications [43,44]. Since Urbach tails are formed due to electron-phonon and electron-defect interactions, the Urbach parameter is strongly dependent on temperature and doping concentration [30,34,45,46]. State-of-the-art models for the Urbach parameter of specific materials are either heuristic or the parameters are directly extracted from experimental observations [30,32–35,39,46,47]. In addition, TMD-based nanodevices typically interface the TMD layers with various oxides. Therefore, TMD device electrons scatter on remote phonons as well [48–50]. Experiments for several TMDs have shown that their Urbach tails strongly depend on the oxide type [51,52]. Different scattering mechanisms can interfere with each other and impact the electronic density of states rendering it hard to estimate without detailed calculations [31,53,54]. This is further complicated by the

\*prasad25081990@gmail.com

strong dependence of electronic and scattering properties in TMD systems on the number of atomic layers and their environment [49,55,56]. Therefore, this work predicts Urbach parameters for MoS<sub>2</sub>, WS<sub>2</sub>, and WSe<sub>2</sub> layer systems as a function of layer thickness, temperature, doping concentration, and oxide type (comprising HfO<sub>2</sub>, Al<sub>2</sub>O<sub>3</sub>, SiO<sub>2</sub>, and *h*-BN) with density-functional-theory-(DFT) based quantum-transport calculations [57,58] for electronic Green's functions including scattering on various types of phonons, charged impurities, and remote scattering on oxide phonons with NEMO5 [31,59,60]. We delineate the contribution of different scattering mechanisms towards the Urbach parameter and gain insight into its dependence on layer thickness and oxide type. All calculations in this work are based on the nonequilibrium Green's function (NEGF) implementation of NEMO5. NEGF is well suited to analyze Urbach parameters [31,61] since it is a method of choice to predict electronic behavior when incoherent scattering and coherent quantum effects are equally relevant. Electronic, thermal, and optoelectronic systems with nanoscale dimensions or pronounced nonequilibrium conditions are a few such examples [62–69]. This work summarizes the quantum-transport calculations with an easily accessible lookup formula to predict Urbach parameters of MoS<sub>2</sub>, WS<sub>2</sub>, and WSe<sub>2</sub> layer systems as a function of layer thickness, temperature, doping concentration, and oxide type. The presented results and formula enable easy assessments of Urbach parameters and ways to customize them for specific TMD-based device concepts.

## II. SIMULATION APPROACH

All TMD structures considered in this work are represented in their native atomic lattice. Electrons are subatomically resolved with maximally localized Wannier functions (MLWFs) derived from DFT Hamiltonians [19,57]. The process of generating electronic Hamiltonian operators first requires a self-consistent electronic structure calculation with the DFT tool VASP [70] with a convergence criterion of  $10^{-8}$  eV. A momentum mesh of  $5 \times 5 \times 5$  Monkhorst-Pack grid and an energy cutoff of 520 eV is used along with van der Waals force included following Ref. [71]. The applied DFT model is the generalized gradient approximation (GGA) employing the Perdew-Burke-Ernzerhof (PBE) functionals. The resulting DFT Hamiltonian operators are then transformed into a MLWF representation using the Wannier90 software [72–74] with *d* orbitals for the metal sites and *sp*<sup>3</sup>-hybridized orbitals for the chalcogenide sites as the initial projection. The spreading of the Wannier functions is reduced iteratively until it converges to around  $2A^2$ . The atom positions and their corresponding electronic Hamiltonian operator of TMD structures are then imported into NEMO5 for NEGF calculations. All electronic Green's functions are solved in the

self-consistent Born approximation with self-energies representing each incoherent scattering mechanism [scattering of electrons with acoustic phonons (APs), polar optical phonons (POPs), charged impurities (CIs), and remote phonons (RPs) from the oxide]. Since the structures are assumed to be periodic in the transverse *Y* direction (see Fig. 1), the electronic Green's functions and self-energies depend on the electronic energy *E* and in-plane momentum *k*. The corresponding Brillouin zones are resolved with 25 points. All Green's functions and self-energies are matrices with respect to the MLWF orbitals along the  $\vec{x} = (X, Z)$  directions. (see Fig. 1). Each scattering process is modeled with a corresponding retarded and lesser scattering self-energy [53,62]. The imaginary part of the retarded self-energy provides information about the scattering rate of the electrons [75], which gives rise to the band tails. The real part of the retarded self-energies yields an energy shift of electronic states [31,76]. Since this work focuses on the Urbach parameter only, the real part of all retarded scattering self-energies is ignored.

In this work, Green's functions of electrons are explicitly solved, whereas Green's functions of phonons are approximated as plane waves occupied with the equilibrium Bose distribution *N*<sub>ph</sub>. The three acoustic phonon types (LA, TA, ZA) are averaged into a single effective deformation potential and sound velocity. The corresponding self-energy given in Ref. [65] is multiplied by  $3 \times$  accordingly. POPs are modeled with a constant, material-dependent phonon energy  $\hbar\omega_{LO}$ . Scattering on CIs is assumed to be elastic. Scatterings on POP and CI are based on long-range Coulomb interaction and therefore yield nonlocal scattering self-energies [77,78]. To limit the numerical burden of solving self-energies and Green's functions but still faithfully predict the POP and CI scattering, the respective self-energies are approximated to be local and multiplied with a material and device-dependent compensation factor. The detailed expressions for POP and

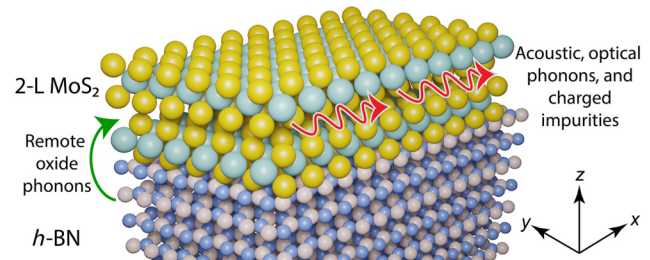


FIG. 1. Representative schematic of the simulated atomic TMD layers placed on top of oxide. Electrons are solved with scattering on acoustic and optical phonons and charged impurities within the TMD layers. In addition, electrons scattering remotely on oxide phonons are included. The *x* direction and *z* direction are resolved in real space, the *y* direction is assumed to be periodic.

CI scattering self-energies and the compensation factor are given in Ref. [31]. The interaction potential of electrons and remote oxide phonons is taken from Ref. [79]. The

resulting lesser and retarded scattering self-energies for electrons remotely scattering on the two surface optical-oxide-phonon modes ( $\nu = 1, 2$ ) are given by

$$\begin{aligned} \Sigma^<(\vec{x}_1, \vec{x}_2, k, E) &= \sum_{\nu} \frac{e^2}{(2\pi)} \frac{\hbar\omega_{SO,\nu}}{2\epsilon_o} \left( \frac{1}{\epsilon_{ox}^{\infty} + \epsilon_s^{\infty}} - \frac{1}{\epsilon_{ox}^s + \epsilon_s^{\infty}} \right) \int dk' I(k, k', \vec{x}_1, \vec{x}_2, z_1, z_2) \\ &\quad \times [N_{ph} G^<(\vec{x}_1, \vec{x}_2, k', E - \hbar\omega_{SO,\nu}) + (1 + N_{ph}) G^<(\vec{x}_1, \vec{x}_2, k', E + \hbar\omega_{SO,\nu})] \\ \Sigma^R(\vec{x}_1, \vec{x}_2, k, E) &= \sum_{\nu} \frac{e^2}{(2\pi)} \frac{\hbar\omega_{SO,\nu}}{2\epsilon_o} \left( \frac{1}{\epsilon_{ox}^{\infty} + \epsilon_s^{\infty}} - \frac{1}{\epsilon_{ox}^s + \epsilon_s^{\infty}} \right) \int dk' I(k, k', \vec{x}_1, \vec{x}_2, z_1, z_2) \\ &\quad \times \left[ (1 + N_{ph}) G^R(\vec{x}_1, \vec{x}_2, l, E - \hbar\omega_{SO,\nu}) + N_{ph} G^R(\vec{x}_1, \vec{x}_2, k', E + \hbar\omega_{SO,\nu}) \right. \\ &\quad \left. + \frac{1}{2} G^<(\vec{x}_1, \vec{x}_2, k', E - \hbar\omega_{SO,\nu}) - \frac{1}{2} G^<(\vec{x}_1, \vec{x}_2, k', E + \hbar\omega_{SO,\nu}) \right. \\ &\quad \left. + i \int \frac{d\tilde{E}}{2\pi} G^<(\vec{x}_1, \vec{x}_2, k', \tilde{E}) \left( Pr \frac{1}{E - \tilde{E} - \hbar\omega_{SO,\nu}} - Pr \frac{1}{E - \tilde{E} + \hbar\omega_{SO,\nu}} \right) \right], \end{aligned} \quad (1)$$

where

$$\begin{aligned} I(k, k', \vec{x}_1, \vec{x}_2, z_1, z_2) &= 2\pi J_0 \left( \sqrt{(k - k')^2 + \zeta^{-2} |\vec{x}_1 - \vec{x}_2|} \right) \\ &\quad \times e^{-\sqrt{(k - k')^2 + \zeta^{-2}}(z_1 + z_2 - 2t)}. \end{aligned} \quad (2)$$

$\hbar\omega_{SO,\nu}$  is the  $\nu^{\text{th}}$  optical-phonon frequency of the underlying oxide,  $\epsilon_{ox}^s$  and  $\epsilon_{ox}^{\infty}$  are the static and infinite frequency dielectric constants of the oxide,  $\epsilon_s^{\infty}$  is the infinite frequency dielectric constant of the TMD. The oxide-phonon modes are considered to decay exponentially into the TMD with  $z_1$  and  $z_2$  the distances of the two electron propagation coordinates from the oxide-semiconductor interface (see Fig. 1).  $t$  is the thickness of the TMD system.  $J_0$  is the Bessel- $J$  function of 0'th order. The electrostatic screening of electrons and holes is represented by  $\zeta$  and calculated with the Lindhard formula [80]

$$\zeta_{\text{Lindhard}} = \left( \frac{e^2}{\epsilon_o \epsilon_s} \frac{-2}{(2\pi)^3} \int d\vec{q} \frac{\partial f}{\partial \epsilon} \Big|_{\epsilon(\vec{q})} \right)^{-1/2}, \quad (3)$$

where  $f$  is the Fermi distribution function and the momentum integral runs over the first Brillouin zone. Scattering on remote phonons is nonlocal and long ranged as well. Similar to the nonlocal POP and CI self-energies, the remote phonon-scattering self-energy is approximated to be local and multiplied with a compensation factor following the approach of Ref. [31]. For later discussion of the results, we define an intrinsic phonon-scattering prefactor (IP) and a remote oxide-phonon-scattering prefactor

(ROP) as

$$P_{\text{IP}} = \frac{\hbar\omega_{\text{LO}}}{2\epsilon_o} \left( \frac{1}{\epsilon_s^{\infty}} - \frac{1}{\epsilon_s^s} \right), \quad (4)$$

$$P_{\text{ROP}} = \sum_{\nu} \frac{\hbar\omega_{SO,\nu}}{2\epsilon_o} \left( \frac{1}{\epsilon_{ox}^{\infty}} - \frac{1}{\epsilon_{ox}^s} \right), \quad (5)$$

where  $\epsilon_s$  is the static dielectric constant of the TMD material. For all the results shown in subsequent sections, the electrons are solved in equilibrium. The electronic Fermi level is determined such that the spatially integrated electron density agrees with the integrated doping concentration to achieve global charge neutrality. Green's functions are solved with the Dyson and Keldysh equations:

$$\begin{aligned} G^R &= (EI - H - \Sigma_{\text{AP}}^R - \Sigma_{\text{POP}}^R - \Sigma_{\text{CI}}^R - \Sigma_{\text{ROP}}^R \\ &\quad - \Sigma_{\text{source}}^R - \Sigma_{\text{drain}}^R)^{-1}, \\ G^< &= G^R (\Sigma_{\text{AP}}^< + \Sigma_{\text{POP}}^< + \Sigma_{\text{CI}}^< + \Sigma_{\text{ROP}}^< \\ &\quad + \Sigma_{\text{source}}^< + \Sigma_{\text{drain}}^<) G^{R\dagger}. \end{aligned} \quad (6)$$

All scattering self-energies are self-consistently solved with Green's functions until the relative particle current variation is less than  $1 \times 10^{-5}$  throughout the device. The source and drain contact self-energies are solved following Ref. [81]. The Urbach parameter is extracted from the exponentially decaying spatially averaged density of states below (above) the conduction (valence) band [31]. The extracted Urbach parameters correspond to the ones measured in transport experiments. In contrast, the parameter

TABLE I. Sound velocity  $v_s$ , material density  $\rho$ , LO phonon frequency ( $\hbar\omega_{\text{LO}}$ ), deformation potentials ( $D$ ), dielectric constants ( $\epsilon_s$  and  $\epsilon_\infty$ ), and IP scattering prefactor for one–four layers of MoS<sub>2</sub>, WS<sub>2</sub>, and WSe<sub>2</sub> used in this work. Parameters are taken from Refs. [55] and [82].

Material	Number of layers	$v_s$ (m/s)	$\rho$ (kg/m <sup>3</sup> )	$\hbar\omega_{\text{LO}}$ (meV)	$D$ (eV/nm)	$\epsilon_s$	$\epsilon_\infty$	IP scattering prefactor
MoS <sub>2</sub>	1	7200	5060	48	4.5	3.8	3.2	0.4069
	2				5.37	5.65	4.8	0.2584
	3				6.25	6.47	5.5	0.2248
	4				7.12	7.3	6.2	0.2004
WS <sub>2</sub>	1	6670	7500	33	3.2	3.65	3.1	0.5847
	2				4.07	5.15	4.37	0.4169
	3				4.95	5.92	5.03	0.3595
	4				5.82	6.7	5.69	0.3187
WSe <sub>2</sub>	1	5550	9320	30	3.2	3.7	3.145	0.6167
	2				4.07	5.3	4.5	0.4337
	3				4.95	6.1	5.18	0.3765
	4				5.82	6.9	5.86	0.3326

extracted from optical measurements are related to excitons, which require a different scattering model accounting for the excitonic interaction. All other material parameters for the TMDs and oxides are taken from Refs. [55,56,82] and listed in Tables I and III.

### III. RESULTS

#### A. Band tails: Intrinsic to the material

Electronic scattering on APs and POPs creates finite density of states above (below) the valence (the conduction) band that decays exponentially into the band gap (see Fig. 2). The slope of this band tail, i.e., the Urbach parameter increases with incoherent scattering of electrons on charged impurities (as also observed in Ref. [31]). The scattering rates are proportional to the imaginary retarded scattering self-energies ( $\Sigma^R$ ) [75]. In the self-consistent Born approximation  $\Sigma^R$  is proportional to the retarded Green's function ( $G^R$ ) [see Eq. (1) and Refs. [31,59]]. Therefore, the strength of the scattering processes that form Urbach tails is determined by the imaginary part of  $G^R$ , i.e., the density of states at the band edges [31]. This is the root cause for the effective-mass dependency of scattering rates in Fermi Golden rule models (see Refs. [77,78]). This results in the Urbach parameter of monolayer MoS<sub>2</sub> valence band being larger than its conduction band as shown in Fig. 2. The effective masses of different valleys and their relative contribution to the Urbach parameter are described in the subsequent paragraph. The phonon- (charged impurity) scattering self-energies are proportional to the phonon number (doping concentration) [31].

Accordingly, Figs. 3(a) and 3(b) show that the Urbach parameters of MoS<sub>2</sub> valence-band electrons increase with doping concentration and temperature. Figures 3(a) and 3(b) also show a reduction of the Urbach parameter with the number of MoS<sub>2</sub> layers. This is due to the

fact the density of states at the top of the valence band of monolayer MoS<sub>2</sub> is larger than the ones of any multilayer MoS<sub>2</sub> system. While the valence-band maximum of monolayer MoS<sub>2</sub> lies at the  $K$  valley with an effective mass of  $0.543m_e$ , the  $K$ -valley energy of monolayer MoS<sub>2</sub> valence bands is only 59 meV higher than the energy of the  $\Gamma$  valley and marginally higher than the polar optical-phonon energy of 48 meV. The phonon occupancy of 48-meV modes at 300 K is high enough for holes at the top of the MoS<sub>2</sub> valence band to experience significant intervalley scattering and to yield a density of states effectively composed of contribution from both valleys. The effective mass of the  $\Gamma$  valley ( $2.886m_e$ ) is significantly larger than the one of the  $K$  valley. Therefore, intervalley scattering raises

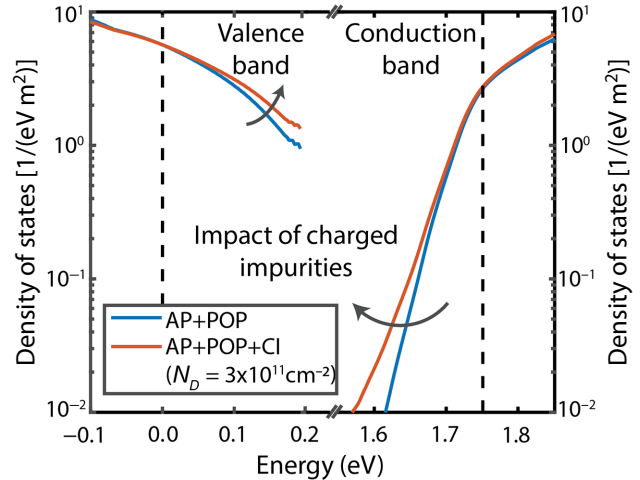


FIG. 2. Density of states of monolayer MoS<sub>2</sub> close to valence- and conduction-band-edges. Scattering on APs and POPs creates Urbach tails into the band gap (blue). Scattering on CIs (red) increases the Urbach tail further. The black dashed lines indicate the valence- and conduction-band-edges without incoherent scattering.

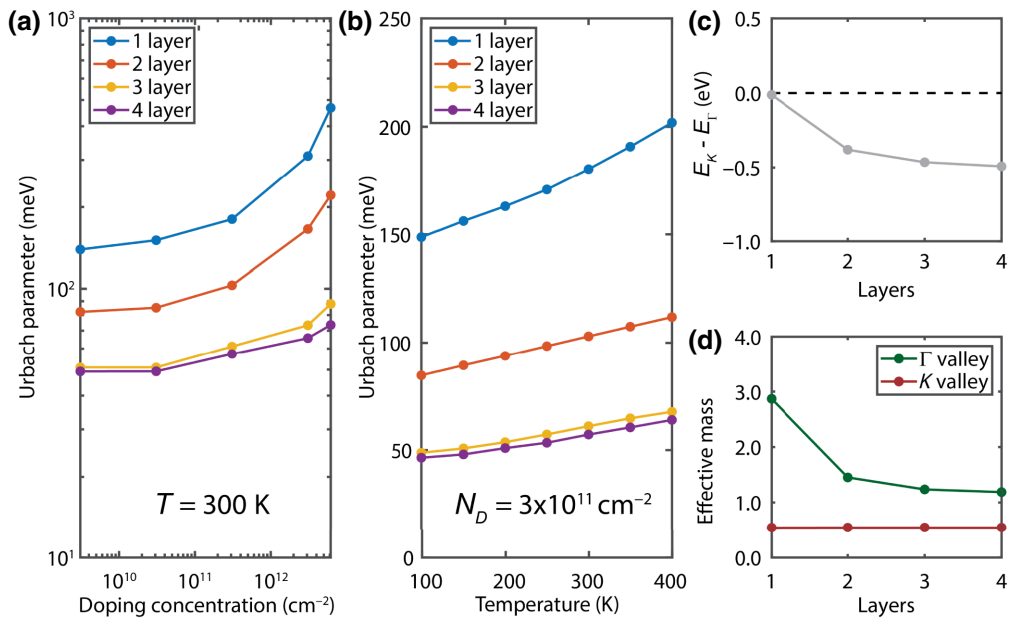


FIG. 3. (a) Urbach parameter of the MoS<sub>2</sub> valence band as a function of doping concentration for a different number of layers at 300 K. With increasing doping concentration, the Urbach parameter increases due to stronger impurity scattering. (b) Urbach parameter of the MoS<sub>2</sub> valence band as a function of temperature for a different number of layers at a doping concentration of  $3 \times 10^{11} \text{ cm}^{-2}$ . With increasing temperature, the Urbach parameter increases due to stronger phonon scattering. Both (a) and (b) show smaller Urbach parameters with larger number of layers because of the reduction of valence-band-edge density of states with more layers: only monolayer MoS<sub>2</sub> exhibits degenerate valence-band  $K$  and  $\Gamma$  valleys as depicted with their energy differences in (c). The density of states of the  $\Gamma$  valley is proportional to its effective mass, which reduces with the number of MoS<sub>2</sub> layers, shown in (d).

the effective density of states of monolayer MoS<sub>2</sub> holes and the corresponding Urbach parameter. This effective degeneracy of  $K$  and  $\Gamma$  valleys is lifted as soon as more than one layer of MoS<sub>2</sub> is present [see Fig. 3(c)]. The effective mass of the  $\Gamma$  valley, i.e., the highest valence-band valley of multilayer MoS<sub>2</sub> systems, and with it the density of

states at the top of the valence band declines continuously with the number of layers with the steepest decline happening between monolayer and bilayer [see Fig. 3(d)]. That is why adding a second MoS<sub>2</sub> layer gives the largest reduction in the Urbach parameter. In addition, the polar optical-phonon-scattering potential decreases with larger

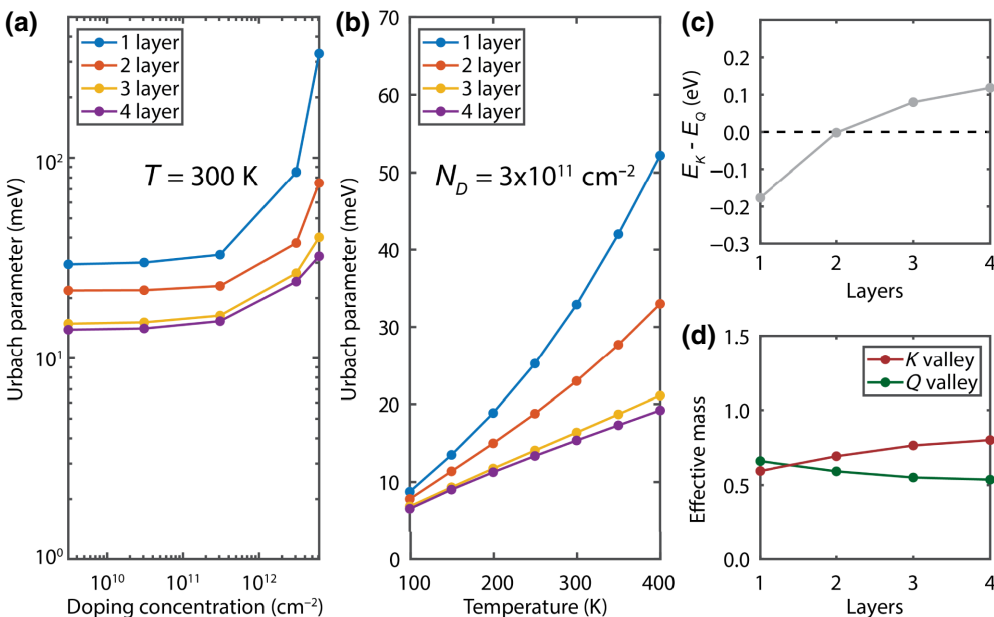


FIG. 4. Similar to Fig. 3, the Urbach parameter of the MoS<sub>2</sub> conduction band as a function of doping concentration (a) and temperature (b). Differing from the valence-band results of Fig. 3, the  $K$  and  $Q$  valleys are degenerate in the bilayer case, [see (c)] and the conduction-band-edge effective mass has a relatively small layer thickness dependence as shown in (d). In spite of the bilayer valley degeneracy, the Urbach parameter still decreases monotonously with the number of layers, since the reduction in scattering potential of the bilayer overcompensates its increase in band-edge density of states (see Table I).

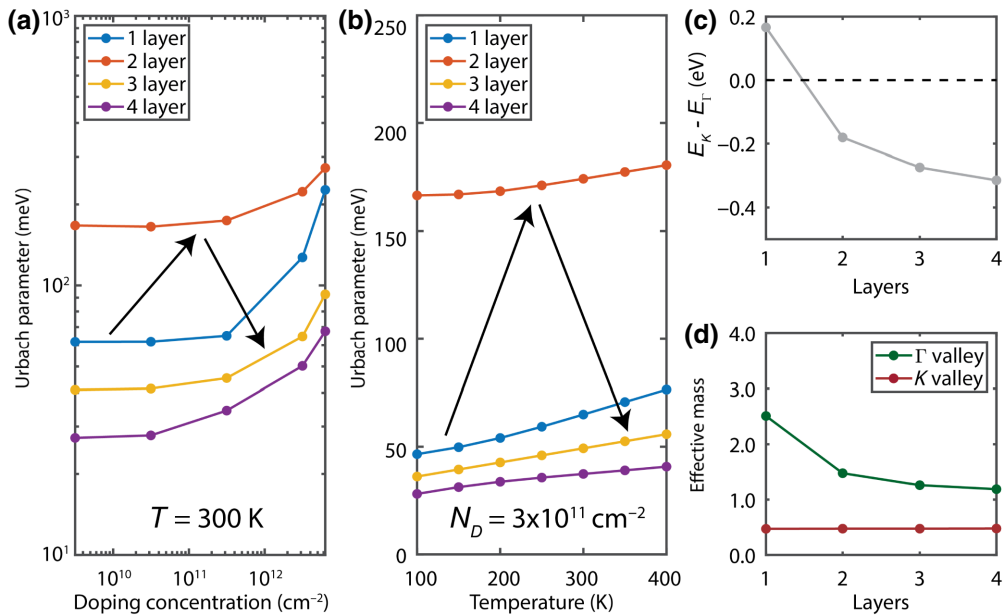


FIG. 5. (a) Urbach parameter of the  $\text{WS}_2$  valence band as a function of doping concentration for a different number of layers at 300 K (a) and as a function of temperature for a doping density of  $3 \times 10^{11} \text{ cm}^{-2}$ . Similar to the valence-band Urbach parameter of  $\text{MoS}_2$  (Fig. 3), the Urbach parameter of  $\text{WS}_2$  increases with doping concentration and temperature. The energy of  $K$  valleys exceed those of the  $\Gamma$  valleys only for monolayer  $\text{WS}_2$  as shown in (c). The transition of the valence-band-edge from  $K$  to  $\Gamma$  valley and the large difference of  $K$ - and  $\Gamma$ -valley effective masses [shown in (d)] cause a maximum of the  $\text{WS}_2$  band-edge density of states and accordingly a maximum of the Urbach parameter for the bilayer configuration (indicated with arrows).

dielectric constants [31,65,83], which has been observed to increase in thicker  $\text{MoS}_2$  layers [55,82]. It is worthwhile to mention that we also observe the decreasing impact of scattering in thicker ultrathin bodies of III-V materials in Ref. [31].

The conduction band of  $\text{MoS}_2$  has a similar dependence on doping concentration and temperature as the

valence band [see Figs. 4(a) and 4(b)]. However, the conduction-band valleys  $K$  and  $Q$  are degenerate only in the bilayer case [see Fig. 4(c)]. In spite of the expected increase in band-edge density of states and with it an increase of the conduction-band Urbach parameter of the bilayer  $\text{MoS}_2$ , the Urbach parameter shows a monotonous decrease with the number of  $\text{MoS}_2$  layers [see Figs. 4(a)

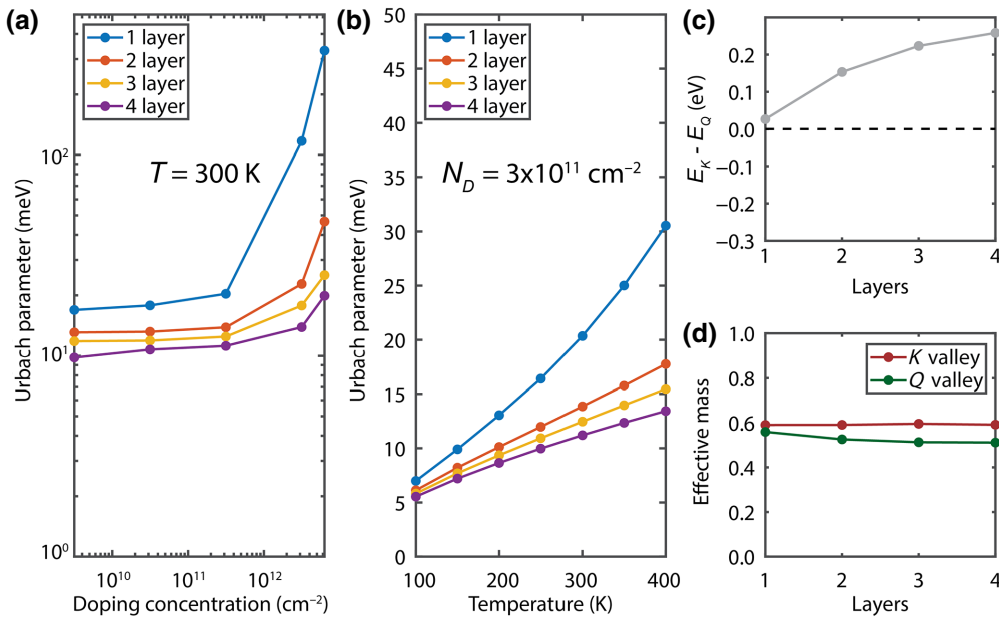


FIG. 6. (a) Urbach parameter of the  $\text{WS}_2$  conduction band as a function of doping concentration (a) and temperature (b) similar for the conduction band of  $\text{MoS}_2$  in Fig. 4. The Urbach parameter declines with increasing number of layers mainly due to the reduction of the scattering potential (see Table I), since neither valley degeneracy in (c) nor the valley effective mass in (d) changes significantly with the number of layers.

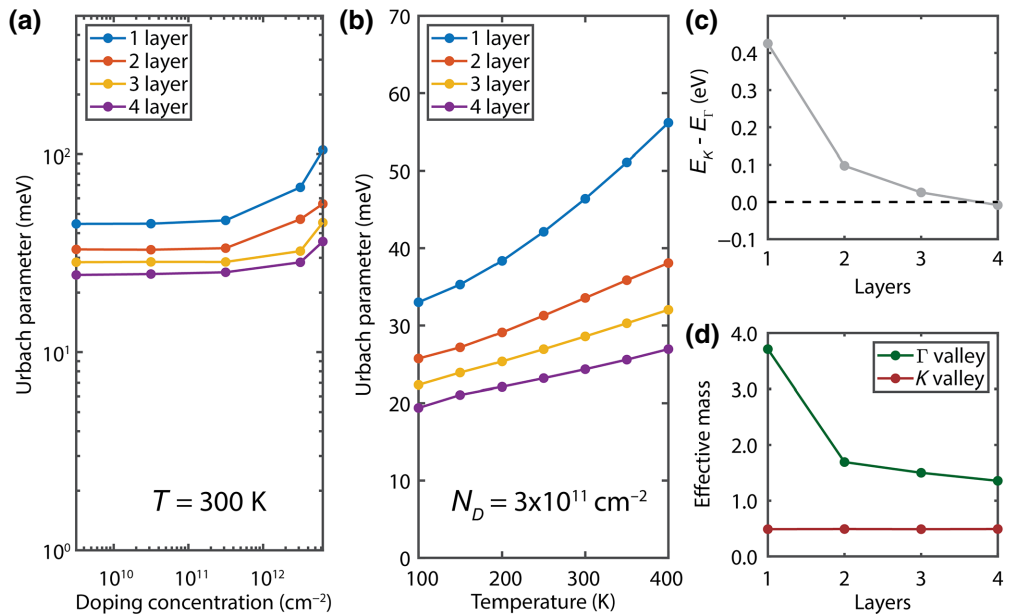


FIG. 7. (a) Urbach parameter of the WSe<sub>2</sub> valence band as a function of doping concentration for a different number of layers at 300 K. With increasing doping concentration, the Urbach parameter increases due to stronger impurity scattering. (b) Urbach parameter of the WSe<sub>2</sub> valence band as a function of temperature for a different number of layers at a doping concentration of  $3 \times 10^{11} \text{ cm}^{-2}$ . With increasing temperature, the Urbach parameter increases due to stronger phonon scattering. Both (a) and (b) show smaller Urbach parameters with a larger number of layers because of the reduction of valence-band-edge density of states with more layers: only four-layer WSe<sub>2</sub> exhibits degenerate valence-band  $K$  and  $\Gamma$  valleys as depicted with their energy differences in (c). Otherwise, the  $\Gamma$  valley contributes only to the conduction. The density of states of the  $\Gamma$  valley is proportional to its effective mass, which reduces with the number of WSe<sub>2</sub> layers, shown in (d).

and 4(b)]. This is due to a significant reduction of the calculated scattering self-energy prefactor of polar optical-phonon-scattering from monolayer to bilayer MoS<sub>2</sub> (see Table I). Overall, the conduction-band Urbach parameters of MoS<sub>2</sub> layers are lower than those of the valence

band due the lower conduction-band effective masses [see Fig. 4(d)].

The valence-band Urbach parameters of WS<sub>2</sub> layers in Figs. 5(a) and 5(b) show similar changes with doping concentration and temperature as the MoS<sub>2</sub> valence-band

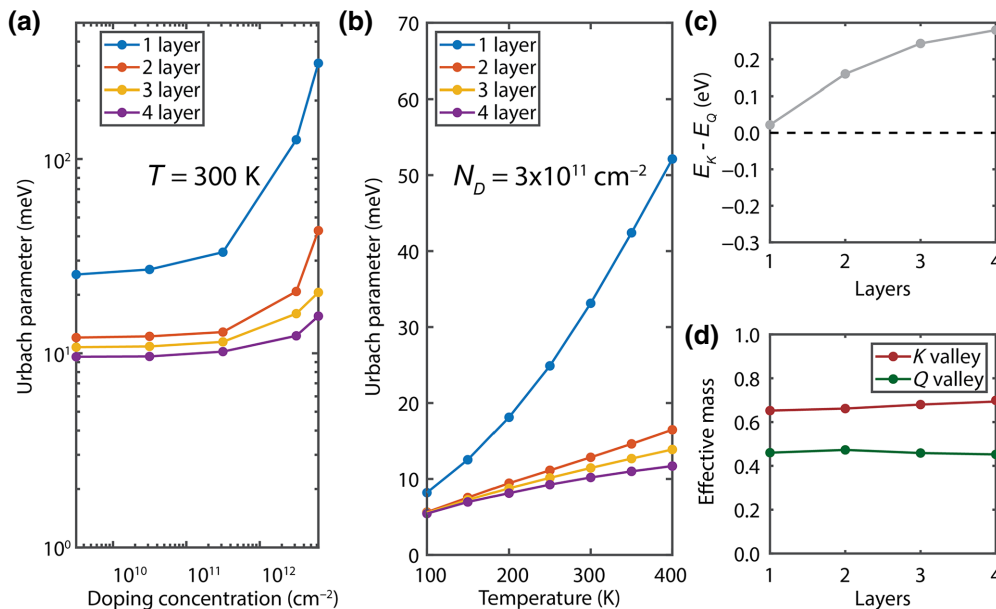


FIG. 8. (a) Urbach parameter of the WSe<sub>2</sub> conduction band as a function of doping concentration (a) and temperature (b) similar to the conduction band of WSe<sub>2</sub> in Fig. 8. The Urbach parameter declines with increasing number of layers mainly due to the reduction of the scattering potential (see Table I), since neither valley degeneracy in (c) nor the valley effective mass in (d) changes significantly with the number of layers.

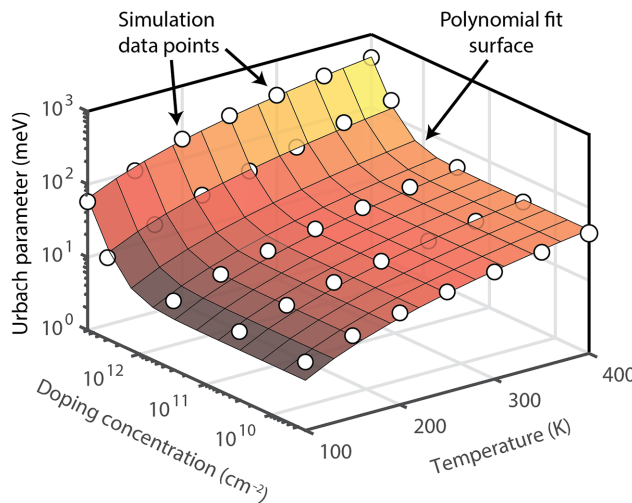


FIG. 9. Urbach parameter as a function of doping concentration and temperature for monolayer MoS<sub>2</sub>. The white circles represent the simulation data points and the contour represents its least-squares polynomial fit. The fit parameters for this and all other systems are given in Table II.

results of Fig. 3. However, the Urbach parameter is largest for bilayer WS<sub>2</sub>. This is due to a transition of the valence-band-edge from  $K$  to  $\Gamma$  valley when more than one layer of

WS<sub>2</sub> is present [see Fig. 5(c)]. Given the large difference of  $K$ - and  $\Gamma$ -valley effective masses [see Fig. 5(d)], this transition causes a maximum in the valence-band-edge density of states and therefore a maximum in the scattering strength for bilayer WS<sub>2</sub>. Accordingly, the Urbach parameter follows this trend [indicated with arrows in Figs. 5(a) and 5(b)]. WS<sub>2</sub> with more than two layers show the similar reduction in the Urbach parameter as discussed already for MoS<sub>2</sub> in Fig. 3.

The conduction-band Urbach parameter of WS<sub>2</sub> (see Fig. 6) is very similar to the one of MoS<sub>2</sub> (see Fig. 4) in its overall dependence on doping and temperature. The scattering potential of the conduction band of WS<sub>2</sub> and with it the Urbach parameter decays with the number of layers (see Table I). Although the conduction band  $K$  and  $Q$  valleys of monolayer WS<sub>2</sub> are close enough in energy to allow for intervalley scattering, the masses of  $K$  and  $Q$  valleys are very similar. Thus, neither significant effective-mass changes nor valley degeneracies influence the Urbach-parameter behavior for WS<sub>2</sub> conduction bands. The same is true for valence and conduction bands of WSe<sub>2</sub> layers as shown in Figs. 7 and 8.

For completeness and to ease the estimation of the Urbach parameter as a function of doping concentration, temperature, layer thickness, and material, all calculated Urbach parameters are input to a polynomial fit given by

TABLE II. Parameters for predicting the Urbach tail with Eq. (7) as a function of temperature and doping concentration for MoS<sub>2</sub>, WS<sub>2</sub>, and WSe<sub>2</sub> along with the  $R^2$  deviation from the calculated quantum transport result. The parameters are determined with the MATLAB curve fitting toolbox [84].

Material	Band type	Number of layers	$a$	$b$	$p$	$q$	$r$	$R^2$ fit value
MoS <sub>2</sub>	Valence	1	149.57	61.162	0.1461	0.8073	0.9078	0.9955
		2	82.981	39.460	0.1116	0.73851	0.6793	0.9978
		3	50.096	14.623	0.1014	1.3003	0.4714	0.9817
		4	49.101	0.1101	0.1002	3.7729	2.3337	0.9271
	Conduction	1	30.567	5.7612	1.6752	1.4527	2.1574	0.9965
		2	22.461	2.4506	1.0747	1.6788	1.6752	0.9988
		3	15.368	2.9972	0.8734	0.0885	1.1907	0.9923
		4	48.497	1.8010	0.0590	6.5438	0.3661	0.9009
WS <sub>2</sub>	Valence	1	63.210	11.144	0.4238	1.3126	1.5879	0.9951
		2	172.43	18.337	0.1102	0.4899	0.8087	0.9222
		3	40.343	12.360	0.2296	0.9083	0.4475	0.9848
		4	27.545	13.102	0.1408	0.8728	0.5770	0.9782
	Conduction	1	17.814	15.216	1.4801	1.0604	1.6482	0.9982
		2	13.449	1.2230	0.7822	0.8175	1.8035	0.9970
		3	12.046	1.3597	0.7226	0.0675	1.2610	0.9930
		4	10.196	1.0997	0.4620	0	1.2088	0.9721
WSe <sub>2</sub>	Valence	1	45.762	4.3223	0.3396	1.0847	1.4928	0.9797
		2	33.271	0.8838	0.2733	0	1.1190	0.9129
		3	28.843	0.0825	0.2060	3.0934	2.8990	0.9810
		4	24.699	0.5682	0.2214	1.7593	1.6473	0.9564
	Conduction	1	28.203	18.465	1.4141	1.0200	1.4832	0.9990
		2	12.450	1.0889	0.7411	0.8994	1.8314	0.9936
		3	10.684	2.1195	0.6217	0	0.8655	0.9917
		4	9.2162	1.6687	0.3946	0	0.7384	0.9311

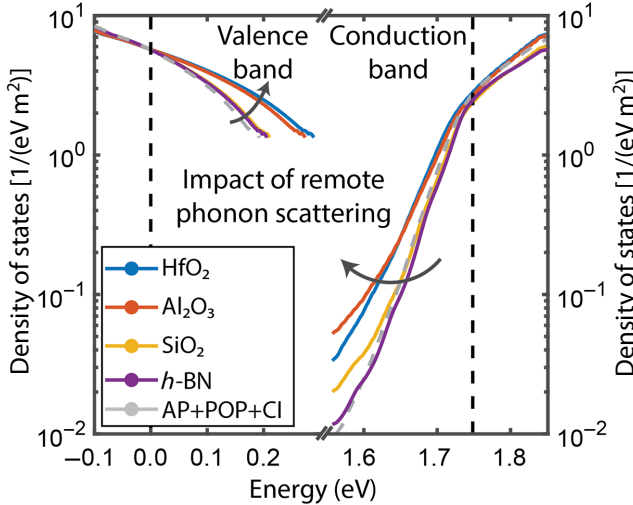


FIG. 10. Density of states of monolayer MoS<sub>2</sub> when exfoliated on various dielectric materials, close to valence- and conduction-band-edges (solid lines). The remote scattering on the dielectric material phonons increases the Urbach tail compared to the intrinsic value of monolayer MoS<sub>2</sub> (gray dashed lines). The impact of the dielectric material phonon scattering follows the same order that is given in Table III, i.e., the strength of the remote phonon-scattering prefactor. The black dashed lines indicate the valence- and conduction-band-edges without incoherent scattering.

$$\text{Urbach}(T, N_D) = a(T/300)^p + b(T/300)^q(N_D/1e12)^r. \quad (7)$$

Figure 9 exemplifies this fit for the conduction-band Urbach parameter of MoS<sub>2</sub>. Since the Urbach parameter depends nonmonotonically on the number of layers, the least-squares fitting is performed for each layer separately. The fit parameters of all considered TMD systems together with their  $R^2$  fit values can be found in Table II.

### B. Band tails: Impacted by dielectric materials

In typical TMD-based nanodevices, the TMD layers are capped with dielectric materials. The remote scattering on phonons in those dielectric materials contribute significantly to the Urbach band tail, as shown in Fig. 10.

The relative impact of remote scattering on phonons in the dielectric materials is directly proportional to the

scattering self-energy prefactor listed in Table III. This prefactor is determined by the difference of the dielectric constants and the energies of the soft optical-phonon modes [see Eq. (1)]. It is worthwhile to mention, HfO<sub>2</sub> has a large scattering impact given its high difference in dielectric constants and the comparably low soft optical-phonon-mode energies. Following the same arguments, the low scattering contributions of h-BN and SiO<sub>2</sub> originate in their high phonon-mode energies and small difference in their dielectric constants.

Figure 11 shows how the ROP scattering impacts the Urbach parameter more in thinner TMD systems than in the thicker ones. This is due to the smaller spatial confinement in larger TMD systems, which allows the charge density in the TMD layers to move farther away from the insulator-TMD interface. Accordingly, the difference in the contributions of the various insulators decreases with increasing TMD thickness. Beyond three layers, the Urbach parameter starts to saturate and slowly approaches the intrinsic value of the respective TMD. As seen already in Fig. 10, the Urbach parameters are consistently higher for Al<sub>2</sub>O<sub>3</sub> and HfO<sub>2</sub> due to their strong ROP scattering potentials.

It is worth mentioning that a similar trend for mobility is observed in Refs. [50,56] for capped TMD systems with HfO<sub>2</sub>/MoS<sub>2</sub> and Al<sub>2</sub>O<sub>3</sub>/MoS<sub>2</sub> exhibiting the strongest suppression of mobility (strong scattering) and SiO<sub>2</sub>/MoS<sub>2</sub> exhibiting the weakest suppression of mobility (weak scattering) in comparison to the vacuum case. In addition, Ref. [50] demonstrates increasing mobility with increasing MoS<sub>2</sub> thickness and saturation to the bulk value around five layers similar to our observed variation of Urbach parameter with the number of layers for each type of oxide.

To roughly benchmark our simulation results against experimental data, we extract the Urbach parameters from several published PL measurements. Note that a direct comparison with the calculated values of this work cannot be quantitative, since all the predicted Urbach parameters of this work are transport band tails, which are known to deviate from the optical, excitonic band tails [85]. We compute the Urbach parameter from the PL spectrum of experimental results by extracting the slope below the band edge. Reference [51] for the conduction band of monolayer MoS<sub>2</sub> exfoliated on SiO<sub>2</sub> presents an Urbach parameter

TABLE III. Soft optical-phonon frequencies ( $\hbar\omega_{SO,1}$  and  $\hbar\omega_{SO,2}$ ), static and infinite frequency dielectric constants of the oxides used in this work taken from Ref. [56] along with the respective ROP scattering prefactors.

Oxide	$\hbar\omega_{SO,1}$ (meV)	$\hbar\omega_{SO,2}$ (meV)	$\epsilon_s$	$\epsilon_\infty$	ROP scattering prefactor
HfO <sub>2</sub>	12.40	48.35	23.00	5.03	3.6363
Al <sub>2</sub> O <sub>3</sub>	48.18	71.41	12.53	3.20	2.9231
SiO <sub>2</sub>	55.60	138.10	3.90	2.50	1.0478
h-BN	93.07	179.10	5.09	4.10	0.1159

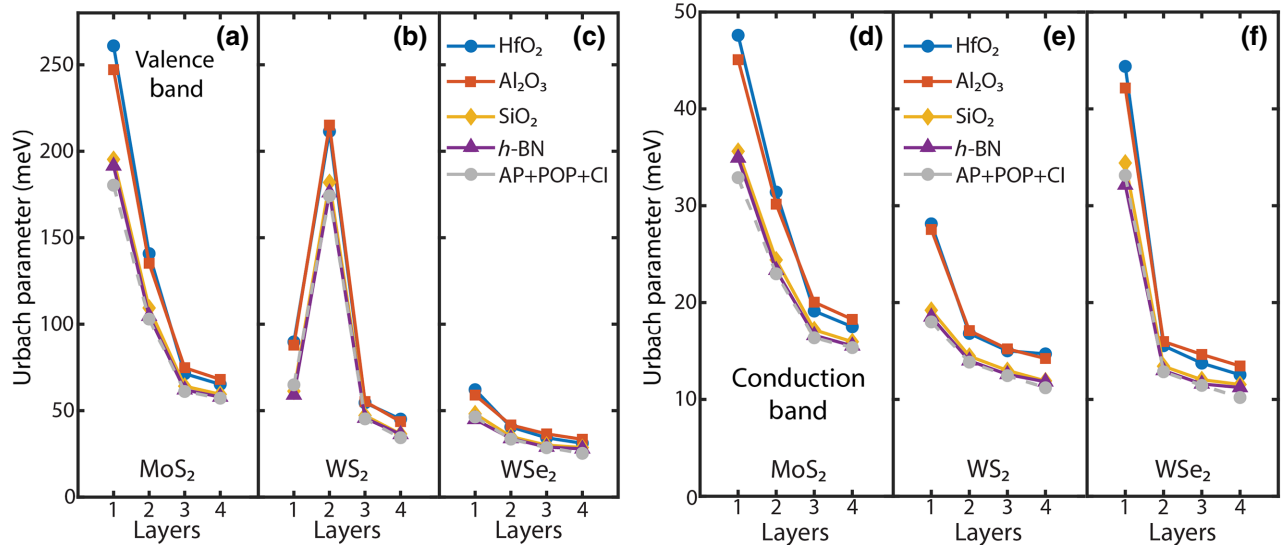


FIG. 11. Conduction-band (a)–(c) and valence-band (d)–(f) Urbach parameters of  $\text{MoS}_2$ ,  $\text{WS}_2$ , and  $\text{WSe}_2$  systems capped with  $\text{HfO}_2$  (dots),  $\text{Al}_2\text{O}_3$  (squares),  $\text{SiO}_2$  (diamonds), or  $h\text{-BN}$  (triangles) along with their intrinsic values (gray dashed lines). As the TMD thickness increases, the maximum of the electron density is located farther from the semiconductor-insulator interface resulting in bands and their Urbach parameters being less affected by the remote scattering on oxide phonons.  $\text{HfO}_2$  and  $\text{Al}_2\text{O}_3$  increase the Urbach parameter more than the other substrates due to their large scattering potentials (see also Fig. 10). Bilayer  $\text{WS}_2$  valence bands show an elevated Urbach parameter due to a transition of the valence-band maximum from the  $K$  to the  $\Gamma$  valley at that layer thickness.

of 40.06 meV before and 30.62 meV after the chemical removal of native defects. Monolayer  $\text{MoS}_2$  fabricated as a type-II heterointerface with perylene in Ref. [86] shows 46.04 meV and 52.94 meV conduction-band Urbach parameter for two perylene hosts—one providing a clean interface and the other hosting trap states, respectively. Reference [52] lists a conduction-band tail parameter of 30.04 meV for monolayer  $\text{MoS}_2$ - $\text{WSe}_2$  van der Waals heterostructure. All the above values correlate well with the findings in Fig. 11.

#### IV. CONCLUSION

Quantum-transport calculations of electrons in TMD systems are used to predict the formation of band tails due to scattering on phonons, charged impurities, and remote scattering on substrate dielectric phonons. All materials are atomically resolved, electronic Hamiltonian operators are based on DFT, and incoherent, nonlocal scattering is modeled in self-consistent Born approximation. It is shown that the Urbach band-tail parameter strongly depends on temperature, impurity concentration and TMD layer thickness as well as on the type of dielectric substrate. The details of the Urbach parameter depend on a balance of valley degeneracies, scattering potentials, and phonon occupancies. This can result in nonmonotonic behavior of the Urbach parameter as seen in  $\text{WS}_2$ . To ease reproducibility of the sophisticated quantum-transport calculations, we present analytical approximations to the observed Urbach-parameter predictions. These analytical formula allow fast

assessments on how far the band tails are tunable within a given TMD-based device concept. Among the dielectric materials considered,  $\text{Al}_2\text{O}_3$  and  $\text{HfO}_2$  are shown to contribute strongest to the remote phonon-scattering-enhanced band tails. With increasing TMD-layer count, electrons spread farther away from the dielectric and thus the contribution of remote scattering on dielectric phonons decreases. Monolayer  $\text{MoS}_2$  results agree well with published observations in experiments.

#### ACKNOWLEDGMENTS

James Charles and Tillmann Kubis acknowledge support by the Silvaco Inc. This research is supported in part through computational resources provided by Information Technology at Purdue, West Lafayette, Indiana. The authors acknowledge the Texas Advanced Computing Center (TACC) at The University of Texas at Austin for providing HPC resources that have contributed to the research results reported within this paper. This research uses resources of the Oak Ridge Leadership Computing Facility, which is a DOE Office of Science User Facility supported under Contract No. DEAC05-00OR22725. Prasad Sarangapani acknowledges Purnima Padmanabhan for helping with the figures.

- Two-dimensional atomic crystals, *Proc. National Acad. Sci.* **102**, 10451 (2005).
- [2] Qing Hua Wang, Kourosh Kalantar-Zadeh, Andras Kis, Jonathan N. Coleman, and Michael S. Strano, Electronics and optoelectronics of two-dimensional transition metal dichalcogenides, *Nat. Nanotechnol.* **7**, 699 (2012).
- [3] Deep Jariwala, Vinod K. Sangwan, Lincoln J. Lauhon, Tobin J. Marks, and Mark C. Hersam, Emerging device applications for semiconducting two-dimensional transition metal dichalcogenides, *ACS Nano* **8**, 1102 (2014).
- [4] Kin Fai Mak and Jie Shan, Photonics and optoelectronics of 2D semiconductor transition metal dichalcogenides, *Nat. Photonics* **10**, 216 (2016).
- [5] Sajedeh Manzeli, Dmitry Ovchinnikov, Diego Pasquier, Oleg V. Yazyev, and Andras Kis, 2D transition metal dichalcogenides, *Nat. Rev. Mater.* **2**, 17033 (2017).
- [6] Sujay B. Desai, Surabhi R. Madhvapathy, Angada B. Sachid, Juan Pablo Llinas, Qingxiao Wang, Geun Ho Ahn, Gregory Pitner, Moon J. Kim, Jeffrey Bokor, and Chenming Hu, *et al.*, MoS<sub>2</sub> transistors with 1-nanometer gate lengths, *Science* **354**, 99 (2016).
- [7] Vitaly Podzorov, M. E. Gershenson, C.h. Kloc, R. Zeis, and E. Bucher, High-mobility field-effect transistors based on transition metal dichalcogenides, *Appl. Phys. Lett.* **84**, 3301 (2004).
- [8] Leitao Liu, S. Bala Kumar, Yijian Ouyang, and Jing Guo, Performance limits of monolayer transition metal dichalcogenide transistors, *IEEE Trans. Electron Devices* **58**, 3042 (2011).
- [9] C. Huyghebaert, T. Schram, Q. Smets, T. Kumar Agarwal, D. Verreck, S. Brems, A. Phommahaxay, D. Chiappe, S. El Kazzi, and C. Lockhart de la Rosa, *et al.*, in *2018 IEEE International Electron Devices Meeting (IEDM)* (IEEE, 2018), p. 22.
- [10] Rui Cheng, Dehui Li, Hailong Zhou, Chen Wang, Anxiang Yin, Shan Jiang, Yuan Liu, Yu Chen, Yu Huang, and Xiangfeng Duan, Electroluminescence and photocurrent generation from atomically sharp WSe<sub>2</sub>/MoS<sub>2</sub> heterojunction *p–n* diodes, *Nano Lett.* **14**, 5590 (2014).
- [11] Britton W. H. Baugher, Hugh O. H. Churchill, Yafang Yang, and Pablo Jarillo-Herrero, Optoelectronic devices based on electrically tunable *p–n* diodes in a monolayer dichalcogenide, *Nat. Nanotechnol.* **9**, 262 (2014).
- [12] Xing Zhou, Xiaozong Hu, Jing Yu, Shiyuan Liu, Zhaowei Shu, Qi Zhang, Huiqiao Li, Ying Ma, Hua Xu, and Tianyou Zhai, 2D layered material-based van der Waals heterostructures for optoelectronics, *Adv. Funct. Mater.* **28**, 1706587 (2018).
- [13] Jie Gu, Biswanath Chakraborty, Mandeep Khatoniar, and Vinod M. Menon, A room-temperature polariton light-emitting diode based on monolayer WS<sub>2</sub>, *Nat. Nanotechnol.* **14**, 1024 (2019).
- [14] Ya-Qing Bie, Gabriele Grossos, Mikkel Heuck, Marco M. Furchi, Yuan Cao, Jiabao Zheng, Darius Bunandar, Effren Navarro-Moratalla, Lin Zhou, and Dmitri K. Efetov, *et al.*, A molybdenum-based light-emitting diode and photodetector for silicon photonic integrated circuits, *Nat. Nanotechnol.* **12**, 1124 (2017).
- [15] Weihao Zheng, Ying Jiang, Xuelu Hu, Honglai Li, Zhouxiao Song, Xiao Wang, and Anlian Pan, Light emission properties of 2D transition metal dichalcogenides: Fundamentals and applications, *Adv. Opt. Mater.* **6**, 1800420 (2018).
- [16] Meng-Lin Tsai, Sheng-Han Su, Jan-Kai Chang, Dung-Sheng Tsai, Chang-Hsiao Chen, Chih-I. Wu, Lain-Jong Li, Lih-Juann Chen, and Jr-Hau He, Monolayer MoS<sub>2</sub> heterojunction solar cells, *ACS Nano* **8**, 8317 (2014).
- [17] Uttiya Dasgupta, Soumyo Chatterjee, and Amlan J. Pal, Thin-film formation of 2D MoS<sub>2</sub> and its application as a hole-transport layer in planar perovskite solar cells, *Sol. Energy Mater. Sol. Cells* **172**, 353 (2017).
- [18] Xi Yang, Weifei Fu, Wenqing Liu, Jinghua Hong, Yu Cai, Chuanhong Jin, Mingsheng Xu, Haibo Wang, Deren Yang, and Hongzheng Chen, Engineering crystalline structures of two-dimensional MoS<sub>2</sub> sheets for high-performance organic solar cells, *J. Mater. Chem. A* **2**, 7727 (2014).
- [19] Kuang-Chung Wang, Teodor K. Stanev, Daniel Valencia, James Charles, Alex Henning, Vinod K. Sangwan, Aritra Lahiri, Daniel Mejia, Prasad Sarangapani, and Michael Povolotskyi, *et al.*, Control of interlayer physics in 2H transition metal dichalcogenides, *J. Appl. Phys.* **122**, 224302 (2017).
- [20] Andreas Pospischil and Thomas Mueller, Optoelectronic devices based on atomically thin transition metal dichalcogenides, *Appl. Sci.* **6**, 78 (2016).
- [21] Shahriar Memaran, Nihar R. Pradhan, Zhengguang Lu, Daniel Rhodes, Jonathan Ludwig, Qiong Zhou, Omotola Ogunsolu, Pulickel M. Ajayan, Dmitry Smirnov, and Antonio I. Fernandez-Dominguez, *et al.*, Pronounced photovoltaic response from multilayered transition-metal dichalcogenides pn-junctions, *Nano Lett.* **15**, 7532 (2015).
- [22] Chul-Ho Lee, Gwan-Hyoung Lee, Arend M. Van Der Zande, Wencho Chen, Yilei Li, Minyong Han, Xu Cui, Ghidewon Arefe, Colin Nuckolls, and Tony F. Heinz, *et al.*, Atomically thin p–n junctions with van der Waals heterointerfaces, *Nat. Nanotechnol.* **9**, 676 (2014).
- [23] Wenjing Zhang, Qixing Wang, Yu Chen, Zhuo Wang, and Andrew T. S. Wee, Van der Waals stacked 2D layered materials for optoelectronics, *2D Mater.* **3**, 022001 (2016).
- [24] Xiaoyun Yu and Kevin Sivula, Layered 2D semiconducting transition metal dichalcogenides for solar energy conversion, *Curr. Opin. Electrochem.* **2**, 97 (2017).
- [25] Kai Wu, Huanhuan Ma, Yunzhi Gao, Wei Hu, and Jinlong Yang, Highly-efficient heterojunction solar cells based on two-dimensional tellurene and transition metal dichalcogenides, *J. Mater. Chem. A* **7**, 7430 (2019).
- [26] Sonali Das, Deepak Pandey, Jayan Thomas, and Tania Roy, The role of graphene and other 2D materials in solar photovoltaics, *Adv. Mater.* **31**, 1802722 (2019).
- [27] Sam Park, Yeonsu Jeong, Hye-Jin Jin, Jun Kyu Park, Hyenam Jang, Sol Lee, Woong Huh, Hyunmin Cho, Hyung Gon Shin, and Kwanpyo Kim, *et al.*, Nonvolatile and neuromorphic memory devices using interfacial traps in two-dimensional WSe<sub>2</sub>/MoTe<sub>2</sub> stack channel, *ACS Nano* **14**, 12064 (2020).
- [28] Guiming Cao, Peng Meng, Jiangang Chen, Haishi Liu, Renji Bian, Chao Zhu, Fucai Liu, and Zheng Liu, 2D material based synaptic devices for neuromorphic computing, *Adv. Funct. Mater.*, 2005443 (2020).

- [29] Lin Wang, Wugang Liao, Swee Liang Wong, Zhi Gen Yu, Sifan Li, Yee-Fun Lim, Xuewei Feng, Wee Chong Tan, Xin Huang, and Li Chen, *et al.*, Artificial synapses based on multiterminal memtransistors for neuromorphic application, *Adv. Funct. Mater.* **29**, 1901106 (2019).
- [30] B. I. Halperin and Melvin Lax, Impurity-band tails in the high-density limit. I. Minimum counting methods, *Phys. Rev.* **148**, 722 (1966).
- [31] Prasad Sarangapani, Yuanchen Chu, James Charles, Gerhard Klimeck, and Tillmann Kubis, Band-Tail Formation and Band-Gap Narrowing Driven by Polar Optical Phonons and Charged Impurities in Atomically Resolved III-V Semiconductors and Nanodevices, *Phys. Rev. Appl.* **12**, 044045 (2019).
- [32] Andreas Schenk, Finite-temperature full random-phase approximation model of band gap narrowing for silicon device simulation, *J. Appl. Phys.* **84**, 3684 (1998).
- [33] Bo E. Sernelius, Band-gap shifts in heavily p-type doped semiconductors of the zinc-blende and diamond type, *Phys. Rev. B* **34**, 5610 (1986).
- [34] B. I. Halperin and Melvin Lax, Impurity-band tails in the high-density limit. II. Higher order corrections, *Phys. Rev.* **153**, 802 (1967).
- [35] Piet Van Mieghem, Theory of band tails in heavily doped semiconductors, *Rev. Mod. Phys.* **64**, 755 (1992).
- [36] Thibault Sohier, Matteo Calandra, and Francesco Mauri, Two-dimensional Fröhlich interaction in transition-metal dichalcogenide monolayers: Theoretical modeling and first-principles calculations, *Phys. Rev. B* **94**, 085415 (2016).
- [37] Hao Lu and Alan Seabaugh, Tunnel field-effect transistors: State-of-the-art, *IEEE J. Electron Devices Soc.* **2**, 44 (2014).
- [38] Sapan Agarwal and Eli Yablonovitch, Band-edge steepness obtained from Esaki/backward diode current–voltage characteristics, *IEEE Trans. Electron Devices* **61**, 1488 (2014).
- [39] Jasper Bizindavyi, Anne S. Verhulst, Quentin Smets, Devin Verreck, Bart Sorée, and Guido Groeseneken, Band-tails tunneling resolving the theory-experiment discrepancy in Esaki diodes, *IEEE J. Electron Devices Soc.* **6**, 633 (2018).
- [40] Jan-Christoph Hebig, Irina Kuhn, Jan Flohre, and Thomas Kirchartz, Optoelectronic properties of  $(\text{CH}_3\text{NH}_3)_3\text{Sb}_2\text{I}_9$  thin films for photovoltaic applications, *ACS Energy Lett.* **1**, 309 (2016).
- [41] Shadia Jamil Ikhmayies and Riyad N. Ahmad-Bitar, A study of the optical bandgap energy and Urbach tail of spray-deposited CDS: In thin films, *J. Mater. Res. Technol.* **2**, 221 (2013).
- [42] J. A. Guerra, J. R. Angulo, S. Gomez, J. Llamoza, L. M. Montañez, A. Tejada, J. A. Töfflinger, A. Winnacker, and R. Weingärtner, The Urbach focus and optical properties of amorphous hydrogenated SiC thin films, *J. Phys. D: Appl. Phys.* **49**, 195102 (2016).
- [43] Arnout Beckers, Farzan Jazaeri, and Christian Enz, Theoretical limit of low temperature subthreshold swing in field-effect transistors, *IEEE Electron Device Lett.* **41**, 276 (2019).
- [44] Arnout Beckers, Dominique Beckers, Farzan Jazaeri, Bertrand Parvais, and Christian Enz, Generalized Boltzmann relations in semiconductors including band tails, *J. Appl. Phys.* **129**, 045701 (2021).
- [45] Sajeev John, Costas Soukoulis, Morrel H. Cohen, and E. N. Economou, Theory of Electron Band Tails and the Urbach Optical-Absorption Edge, *Phys. Rev. Lett.* **57**, 1777 (1986).
- [46] S. C. Jain and D. J. Roulston, A simple expression for band gap narrowing (BGN) in heavily doped Si, Ge, GaAs and  $\text{Ge}_x\text{Si}_{1-x}$  strained layers, *Solid-State Electronics* **34**, 453 (1991).
- [47] Haojun Zhang, Wei Cao, Jiahao Kang, and Kaustav Banerjee, in *Electron Devices Meeting (IEDM), 2016 IEEE International* (IEEE, 2016), p. 30.
- [48] Maarten L. Van de Put, Gautam Gaddemanne, Sanjay Gopalan, and Massimo V. Fischetti, in *2020 International Conference on Simulation of Semiconductor Processes and Devices (SISPAD)* (IEEE), p. 281.
- [49] Debdeep Jena and Aniruddha Konar, Enhancement of Carrier Mobility in Semiconductor Nanostructures by Dielectric Engineering, *Phys. Rev. Lett.* **98**, 136805 (2007).
- [50] Anna Hauber and Stephen Fahy, Scattering of carriers by coupled plasmon-phonon modes in bulk polar semiconductors and polar semiconductor heterostructures, *Phys. Rev. B* **95**, 045210 (2017).
- [51] Matin Amani, Der-Hsien Lien, Daisuke Kiriya, Jun Xiao, Angelica Azcatl, Jiyoung Noh, Surabhi R. Madhvapathy, Rafik Addou, K. C. Santosh, and Madan Dubey, *et al.*, Near-unity photoluminescence quantum yield in  $\text{MoS}_2$ , *Science* **350**, 1065 (2015).
- [52] Hui Fang, Corsin Battaglia, Carlo Carraro, Slavomir Nemšák, Burak Ozdol, Jeong Seuk Kang, Hans A. Bechtel, Sujay B. Desai, Florian Kronast, and Ahmet A. Ünal, *et al.*, Strong interlayer coupling in van der Waals heterostructures built from single-layer chalcogenides, *Proc. National Acad. Sci.* **111**, 6198 (2014).
- [53] Christian Jirauschek and Tillmann Kubis, Modeling techniques for quantum cascade lasers, *Appl. Phys. Rev.* **1**, 011307 (2014).
- [54] G. M. Eliashberg, Interactions between electrons and lattice vibrations in a superconductor, *Sov. Phys. JETP* **11**, 696 (1960).
- [55] Ashok Kumar and P. K. Ahluwalia, Tunable dielectric response of transition metals dichalcogenides  $\text{MX}_2$  ( $\text{M}=\text{Mo, W; X=S, Se, Te}$ ): Effect of quantum confinement, *Phys. B: Condens. Matter* **407**, 4627 (2012).
- [56] Nan Ma and Debdeep Jena, Charge Scattering and Mobility in Atomically Thin Semiconductors, *Phys. Rev. X* **4**, 011043 (2014).
- [57] Áron Szabó, Reto Rhyner, and Mathieu Luisier, Ab initio simulation of single-and few-layer mos 2 transistors: Effect of electron-phonon scattering, *Phys. Rev. B* **92**, 035435 (2015).
- [58] Aryan Afzalian, Ab initio perspective of ultra-scaled CMOS from 2D-material fundamentals to dynamically doped transistors, *npj 2D Mater. Appl.* **5**, 1 (2021).
- [59] James Charles, Prasad Sarangapani, Roksana Golizadeh-Mojarad, Robert Andrawis, Daniel Lemus, Xinchen Guo, Daniel Mejia, James E. Fonseca, Michael Povolotskyi, and Tillmann Kubis, *et al.*, Incoherent transport in NEMO5: Realistic and efficient scattering on phonons, *J. Comput. Electron.* **15**, 1123 (2016).
- [60] Daniel A. Lemus, James Charles, and Tillmann Kubis, Mode-space-compatible inelastic scattering in atomistic

- nonequilibrium Green's function implementations, *J. Comput. Electron.* **19**, 1389 (2020).
- [61] M. Abul Khayer and Roger K. Lake, Effects of band-tails on the subthreshold characteristics of nanowire band-to-band tunneling transistors, *J. Appl. Phys.* **110**, 074508 (2011).
- [62] Roger Lake, Gerhard Klimeck, R. Chris Bowen, and Dejan Jovanovic, Single and multiband modeling of quantum electron transport through layered semiconductor devices, *J. Appl. Phys.* **81**, 7845 (1997).
- [63] Troels Markussen, Antti-Pekka Jauho, and Mads Brandbyge, Electron and phonon transport in silicon nanowires: Atomistic approach to thermoelectric properties, *Phys. Rev. B* **79**, 035415 (2009).
- [64] S.-C. Lee and Andreas Wacker, Nonequilibrium Green's function theory for transport and gain properties of quantum cascade structures, *Phys. Rev. B* **66**, 245314 (2002).
- [65] T. Kubis, C. Yeh, P. Vogl, A. Benz, G. Fasching, and C. Deutsch, Theory of nonequilibrium quantum transport and energy dissipation in terahertz quantum cascade lasers, *Phys. Rev. B* **79**, 195323 (2009).
- [66] Prasad Sarangapani, Cory Weber, Jiwon Chang, Stephen Cea, Michael Povolotskyi, Gerhard Klimeck, and Tillmann Kubis, Atomistic tight-binding study of contact resistivity in si/sige pmos schottky contacts, *IEEE Trans. Nanotechnol.* (2018).
- [67] Yuanchen Chu, Jingjing Shi, Kai Miao, Yang Zhong, Prasad Sarangapani, Timothy S. Fisher, Gerhard Klimeck, Xiulin Ruan, and Tillmann Kubis, Thermal boundary resistance predictions with non-equilibrium Green's function and molecular dynamics simulations, *Appl. Phys. Lett.* **115**, 231601 (2019).
- [68] Junzhe Geng, Prasad Sarangapani, Kuang-Chung Wang, Erik Nelson, Ben Browne, Carl Wordelman, James Charles, Yuanchen Chu, Tillmann Kubis, and Gerhard Klimeck, Quantitative multi-scale, multi-physics quantum transport modeling of GaN-based light emitting diodes, *Physica Status Solidi (a)* **215**, 1700662 (2018).
- [69] Kuang-Chung Wang, Roberto Grassi, Yuanchen Chu, Shree Hari Sureshbabu, Junzhe Geng, Prasad Sarangapani, Xinchen Guo, Mark Townsend, and Tillmann Kubis, Introduction of multi-particle büttiker probes—bridging the gap between drift diffusion and quantum transport, *J. Appl. Phys.* **128**, 014302 (2020).
- [70] Jürgen Hafner, Ab-initio simulations of materials using VASP: Density-functional theory and beyond, *J. Comput. Chem.* **29**, 2044 (2008).
- [71] Tomas Bucko, Jurgen Hafner, Sebastien Lebegue, and Janos G. Angyan, Improved description of the structure of molecular and layered crystals: Ab initio DFT calculations with van der Waals corrections, *J. Phys. Chem. A* **114**, 11814 (2010).
- [72] Nicola Marzari and David Vanderbilt, Maximally localized generalized wannier functions for composite energy bands, *Phys. Rev. B* **56**, 12847 (1997).
- [73] Kristian Sommer Thygesen, Lars Bruno Hansen, and Karsten Wedel Jacobsen, Partly occupied wannier functions: Construction and applications, *Phys. Rev. B* **72**, 125119 (2005).
- [74] Shishir K. Pandey, Ruma Das, and Priya Mahadevan, Layer-dependent electronic structure changes in transition metal dichalcogenides: The microscopic origin, *ACS Omega* **5**, 15169 (2020).
- [75] Andreas Wacker, Semiconductor superlattices: A model system for nonlinear transport, *Phys. Rep.* **357**, 1 (2002).
- [76] Aniello Esposito, Martin Frey, and Andreas Schenk, Quantum transport including nonparabolicity and phonon scattering: Application to silicon nanowires, *J. Comput. Electron.* **8**, 336 (2009).
- [77] Gerald D. Mahan, *Many-Particle Physics* (Springer Science & Business Media, Boston, MA, 2013).
- [78] Carlo Jacoboni, *Theory of Electron Transport in Semiconductors: a Pathway from Elementary Physics to Nonequilibrium Green Functions* Vol. 165 (Springer Science & Business Media, Berlin Heidelberg, 2010).
- [79] Massimo V. Fischetti, Deborah A. Neumayer, and Eduard A. Cartier, Effective electron mobility in si inversion layers in metal–oxide–semiconductor systems with a high- $\kappa$  insulator: The role of remote phonon scattering, *J. Appl. Phys.* **90**, 4587 (2001).
- [80] Jens Lindhard, On the properties of a gas of charged particles, *Dan. Vid. Selsk Mat.-Fys. Medd.* **28**, 8 (1954).
- [81] M. P. Lopez Sancho, J. M. Lopez Sancho, J. M. Lopez Sancho, and J. Rubio, Highly convergent schemes for the calculation of bulk and surface green functions, *J. Phys. F: Metal Phys.* **15**, 851 (1985).
- [82] Zhenghe Jin, Xiaodong Li, Jeffrey T. Mullen, and Ki Wook Kim, Intrinsic transport properties of electrons and holes in monolayer transition-metal dichalcogenides, *Phys. Rev. B* **90**, 045422 (2014).
- [83] Brian K. Ridley, *Quantum Processes in Semiconductors* (Oxford university press, Oxford, England, 2013).
- [84] Inc. The MathWorks, *Curve Fitting Toolbox*, Natick, Massachusetts, United State (2019).
- [85] J. Klein, A. Kerelsky, M. Lorke, M. Florian, F. Sigger, J. Kiemle, M. C. Reuter, T. Taniguchi, K. Watanabe, and J. J. Finley, *et al.*, Impact of substrate induced band tail states on the electronic and optical properties of MoS<sub>2</sub>, *Appl. Phys. Lett.* **115**, 261603 (2019).
- [86] S.k. Md. Obaidulla, Mohammad Rezwan Habib, Yahya Khan, Yuhan Kong, Tao Liang, and Mingsheng Xu, MoS<sub>2</sub> and perylene derivative based type-ii heterostructure: Bandgap engineering and giant photoluminescence enhancement, *Adv. Mater. Interfaces* **7**, 1901197 (2020).